Physica D 239 (2010) 33–43

Contents lists available at ScienceDirect

Physica D

journal homepage: www.elsevier.com/locate/physd

Degenerate discontinuity-induced bifurcations in tapping-mode atomic-force microscopy

Sambit Misra [a], Harry Dankowicz [a,*], Mark R. Paul [b]

[a] Mechanical Science and Engineering, University of Illinois at Urbana-Champaign, Urbana, IL 61801, United States
[b] Mechanical Engineering, Virginia Polytechnic Institute and State University, Blacksburg, VA 24061, United States

ARTICLE INFO

Article history:
Received 10 November 2008
Received in revised form
15 August 2009
Accepted 4 October 2009
Available online 13 October 2009
Communicated by G. Stepan

Keywords:
Tapping-mode
Atomic-force microscopy
Discontinuity mappings
Codimension-two bifurcations
Branch point bifurcation
Isola bifurcation

ABSTRACT

This paper documents the existence of degenerate bifurcation scenarios in the low-contact-velocity dynamics during tapping-mode atomic-force microscopy. Specifically, numerical analysis of a model of the microscope dynamics shows branch point and isola bifurcations associated with the emergence of two families of saddle–node bifurcation points along a branch of low-amplitude oscillations. The paper argues for the origin of the degenerate bifurcations in the existence of a periodic steady-state trajectory that (i) achieves tangential contact with a discontinuity surface in a piecewise smooth model of the cantilever response and (ii) retracts from the surface under variations in either direction along a line segment in parameter space. Specifically, the discontinuity-mapping technique is here rigorously applied to a general situation of such degenerate contact showing the codimension-two nature of these bifurcations for appropriately chosen parameter values. The discontinuity-mapping-based normal form derived here is a novel extension of that derived in Dankowicz and Nordmark (2000) [28] in the case that (ii) does not hold. In addition, the paper includes a quantitative reflection on the relative importance of discontinuities in the attractive and repulsive force components in producing the predicted bifurcations.

1. Introduction

Atomic-force microscopy is a widely used technology for micro- and nanoscale material characterization [1–3]. A commonly employed measurement modality for soft materials (such as those of biological origin) is that of tapping-mode atomic-force microscopy (see [4–9]) as this involves only short, intermittent contact between the tip of an oscillating micro-cantilever and the sample surface. Here, vibrations of the cantilever tip are induced through oscillations of a dither piezo at the cantilever support. The resulting cantilever response is modulated due to the presence of attractive and repulsive tip–sample interaction forces in close proximity to the sample surface [1,10–13]. A significant body of work already exists that deals with the effects of the weak, long-range, attractive and strong, short-range, repulsive tip–sample interaction forces on the dynamics of the oscillating cantilever [14–17]. In particular, this work has theoretically established properties of the cantilever response characteristic of nonlinear dynamical systems, such as changes in the number and stability of steady-state responses; coexistence of multiple stable steady-state trajectories; parameter hysteresis in transitions between different coexisting steady-state trajectories; and chaos (e.g., [18–21]).

The coexistence of multiple stable steady-state trajectories is a source of uncertainty in relating measurements of the cantilever response to variations in the surface properties [13]. As the basins of attraction of each such attractor occupies a subset of state space, noise or disturbances induced during scanning operation may be sufficient to cause transitions between nearby stable oscillation states. Such transitions may be hard to distinguish from those associated with actual changes in surface topography. In addition, whereas low-amplitude, low-contact-velocity oscillations are preferable during imaging of soft materials due to the reduced likelihood of surface damage (e.g., [7,8]), high-amplitude oscillations afford better lateral resolution when imaging hard surfaces common in microelectronic applications [22,23]. Sudden, unexpected transitions between such oscillatory states may therefore compromise sample integrity and/or imaging resolution.

The occurrence of coexistence of stable, high- and low-amplitude steady-state oscillations depends on system parameters, such as the frequency and amplitude of the dither-piezo excitation or the average separation between the cantilever support and the sample surface. Indeed, as reported by San Paulo and García [13] and García and San Paulo [10], while stable low- and high-amplitude oscillations may coexist over a range of average separations for a given excitation amplitude, for higher excitation amplitudes the high-amplitude oscillation may be the only periodic steady-state trajectory over large ranges of average separations. Numerical values for the system parameters characterizing the excitation could

* Corresponding author.
E-mail addresses: danko@illinois.edu (H. Dankowicz), mrp@vt.edu (M.R. Paul).

0167-2789/$ – see front matter © 2009 Elsevier B.V. All rights reserved.
doi:10.1016/j.physd.2009.10.001

therefore be appropriately chosen so as to ensure a persistent low-amplitude cantilever response over a large range of average separations or the absence thereof, depending on the desired oscillatory motion of the cantilever.

Many of the commonly used models for the tip–sample interaction forces are only piecewise smooth with (at least) a discontinuous derivative with respect to tip–sample separation corresponding to the onset of repulsive force interactions. As shown in previously published work by the authors [24], such discontinuities (or suitably smoothed substitutes) are associated with possibly dramatic transitions in the system response in which low-contact-velocity periodic oscillations lose stability or disappear altogether. In recent work [25,26], the analysis of such *discontinuity-induced bifurcations* has been undertaken using the discontinuity-mapping technique, originally introduced by Nordmark [27] in the case of impacting systems and extended to continuous vector field with discontinuous derivatives by Dankowicz and Nordmark [28].

The objective of the current paper is to establish a novel extension of the original formulation from Dankowicz and Nordmark [28]. Of concern here is the case where a low-amplitude oscillation may be found that achieves simple tangential (grazing) contact with a suitably defined discontinuity surface in state space for a critical set of parameter values. Previous results pertain to the common situation in which the oscillatory solution retracts from the discontinuity surface under variations in one direction along a line segment in parameter space but intersects the discontinuity surface under variations in the opposite direction. In contrast, the present analysis focuses on the degenerate situation in which the oscillatory solution retracts from the discontinuity surface under small variations in either direction along the line segment. As established rigorously in the limit of so-called "strong" discontinuities, such a degeneracy is here found to be associated with the occurrence of codimension-two branch point and isola bifurcations (cf. [29]) from which two families of codimension-one saddle–node bifurcations originate. The second contribution of this paper is the application of this theory to a characteristic phenomenology reported in previous work on the atomic-force-microscope cantilever response. In particular, the discussion includes a quantitative reflection on the relative importance of discontinuities in the attractive and repulsive force components in producing the predicted bifurcations.

The paper is organized as follows. Section 2 presents a simple, lumped-parameter, single-mechanical-mode model of the cantilever dynamics based on a commonly used formulation for the tip–sample interaction force. The section includes the results of numerical continuation analysis used to trace families of periodic steady-state trajectories under variations in a set of normalized system parameters. In particular, branch point and isola bifurcation points are both found for different values of the excitation amplitude and equilibrium separation. The discontinuity-mapping-based perturbation analysis is presented in Section 3 (and the Appendix). The practical application of the theory to an example forced oscillator with a piecewise linear spring force demonstrates both the qualitative features of suitably defined bifurcation diagrams as well as quantitative tools for determining the bifurcation behavior based at conditions at grazing. The extent to which the perturbation analysis can be relied upon to accurately capture the numerical phenomenology observed for the cantilever dynamics is explored in Section 4. In particular, it is found that, for the parameter values considered here, the discontinuity in the attractive force components as well as the onset of repulsive force components are both necessary to reproduce the observed bifurcation behavior. Section 5 concludes the paper with a discussion of the plausibility of the discontinuity-mapping-based arguments and the possibility of designing control strategies to prevent the occurrence of the possibly undesirable codimension-two bifurcations.

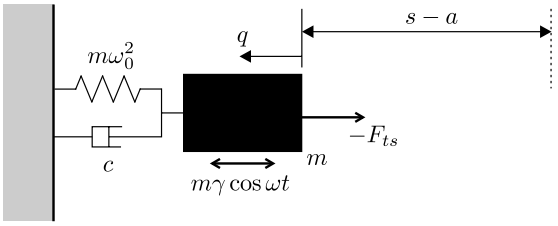

Fig. 1. Schematic lumped-mass model of the cantilever dynamics during tapping-mode operation.

2. A mathematical model

Following García and San Paulo [10], we consider a lumped-parameter, single-mechanical-mode model of the cantilever dynamics during tapping-mode operation as described by the equation

$$m\frac{\mathrm{d}^2q}{\mathrm{d}t^2}+c\frac{\mathrm{d}q}{\mathrm{d}t}+m\omega_0^2q=m\gamma\cos\omega t+F_{ts}\left(q+s\right), \tag{1}$$

where q denotes the effective displacement of the cantilever tip in a direction away from the sample surface, s denotes the average separation between the cantilever support and the sample surface, m denotes the lumped cantilever mass, $m\omega_0^2$ denotes the lumped cantilever stiffness, c represents the intrinsic cantilever damping as well as dissipative interactions with the ambient environment, γ and ω denote the acceleration amplitude and angular frequency of the dither piezo used to excite the cantilever oscillations,

$$F_{ts}:z\longmapsto\begin{cases}-\dfrac{HR}{6z^2}, & z>a\\ -\dfrac{HR}{6a^2}+\dfrac{4}{3}E^*\sqrt{R}\left(a-z\right)^{3/2}, & z\le a\end{cases} \tag{2}$$

is the tip-sample-interaction force function, and t denotes time (cf. Fig. 1). Here, H is the Hamaker constant for the sample surface, R is the cantilever tip radius, E^* is the effective elastic modulus for the contact interactions between the cantilever tip and the sample surface, and a is a characteristic intermolecular distance.

Denote by

$$A_0\stackrel{\mathrm{def}}{=}\frac{m\gamma}{\sqrt{m^2\left(\omega_0^2-\omega^2\right)^2+c^2\omega^2}} \tag{3}$$

the amplitude of the periodic steady-state solution in the absence of the tip–sample interactions and let

$$\mathbf{x}=\begin{pmatrix}x_1\\x_2\\x_3\end{pmatrix}\stackrel{\mathrm{def}}{=}\begin{pmatrix}\dfrac{q}{A_0}\\ \dfrac{1}{A_0\omega_0}\dfrac{\mathrm{d}q}{\mathrm{d}t}\\ \omega t\bmod 2\pi\end{pmatrix}\in\mathbb{R}^2\times\mathbb{S}^1. \tag{4}$$

Differentiation with respect to the rescaled time variable $\tau=\omega_0 t$ then yields the equivalent system of first-order differential equations

$$\frac{\mathrm{d}\mathbf{x}}{\mathrm{d}\tau}=\begin{pmatrix}x_2\\ -Q^{-1}x_2-x_1+\sqrt{\left(1-\tilde\omega^2\right)^2+Q^{-2}\tilde\omega^2}\cos x_3+\tilde F_{ts}\left(x_1+\tilde s\right)\\ \tilde\omega\end{pmatrix}, \tag{5}$$

where

$$\tilde F_{ts}:z\longmapsto\begin{cases}-\dfrac{\sigma_a\tilde a^3}{z^2}, & z>\tilde a\\ -\sigma_a\tilde a+\dfrac{\sigma_r}{\sqrt{\tilde a}}\left(\tilde a-z\right)^{3/2}, & z\le\tilde a,\end{cases} \tag{6}$$

and the nondimensionalized parameters

Table 1
Numerical parameter values characterizing the tip–sample interactions and the lumped behavior of the AFM cantilever (cf. [16,10]).

Parameter	Numerical value
H	7.1×10^{-20} J
R	10 nm
a	0.177 nm
$m\omega_0^2$	40 N/m
E^*	1.09 GPa
Q	400
σ_a	0.532
σ_r	0.0484

$$Q = \frac{m\omega_0}{c}, \qquad \tilde{\omega} = \frac{\omega}{\omega_0}, \qquad \tilde{s} = \frac{s}{A_0}, \qquad \tilde{a} = \frac{a}{A_0}, \tag{7}$$

and

$$\sigma_a = \frac{HR}{6m\omega_0^2 a^3}, \qquad \sigma_r = \frac{4}{3}\frac{E^*\sqrt{Ra}}{m\omega_0^2}. \tag{8}$$

In particular, for sufficiently large $\tilde{s}$, the steady-state response of the cantilever is closely approximated by that of a harmonically excited, damped harmonic oscillator, namely

$$x_1(\tau) = \cos(\tilde{\omega}\tau - \phi), \tag{9}$$

where

$$\cos\phi = \frac{1-\tilde{\omega}^2}{\sqrt{\left(1-\tilde{\omega}^2\right)^2 + Q^{-2}\tilde{\omega}^2}} \tag{10}$$

for $0 < \phi < \pi$. The piecewise smooth, hybrid dynamical system formulated here corresponds to a vector field that is everywhere continuous but with discontinuous first derivative along the discontinuity surface $x_1 + \tilde{s} - \tilde{a} = 0$. The objective of the remainder of this paper is to investigate a class of degenerate changes in the system response induced by the onset of interactions with such a discontinuity.

Using the parameter values shown in Table 1, it is possible to numerically continue the family of steady-state periodic attractors approximated by Eq. (9) under variations in the normalized average separation $\tilde{s}$, intermolecular distance $\tilde{a}$, and excitation frequency $\tilde{\omega}$. The results of several such continuation runs are shown in Fig. 2, where the minimum values of $x_1 + \tilde{s} - \tilde{a}$ along the corresponding steady-state periodic trajectories are parametrized by $\tilde{s}$ and $\tilde{a}$ for $\tilde{\omega} = 1$.

As shown in Fig. 2(a), for large values of $\tilde{a}$ (i.e., small values of the excitation amplitude) the branch of steady-state periodic trajectories extends to small values of $\tilde{s}$, folds back on itself at the point SN_1 and then again at the point SN_2. Also noted in the figure are the points GR_1 and GR_2 corresponding to periodic trajectories with zero minimum values of $x_1 + \tilde{s} - \tilde{a}$, i.e., trajectories that achieve *grazing incidence* with the discontinuity surface $x_1 + \tilde{s} - \tilde{a} = 0$. Of these, GR_1 corresponds to a point of transversal intersection of the family of periodic trajectories with the discontinuity surface under variations in $\tilde{s}$. In contrast, GR_2 is a point of quadratic contact of the family of periodic trajectories with the discontinuity surface under variations in $\tilde{s}$.

Each fold in the branch of periodic trajectories is associated with a change in stability. In particular, points on the middle branch between SN_1 and SN_2 correspond to periodic trajectories that are unstable to arbitrarily small perturbations. In contrast, points on the upper and lower branches (except for a short segment containing the point GR_1) are asymptotically stable for sufficiently small perturbations. The coexistence of two branches of asymptotically stable periodic steady-state oscillations is characteristic of the phenomenon of bistability documented throughout the recent atomic-force-microscopy literature.

As shown in Fig. 2(b), for intermediate values of $\tilde{a}$ the branch of steady-state periodic trajectories reaches a fold at the point SN_4 at an intermediate value of $\tilde{s}$ and then folds back on itself again at the point SN_2. For the same value of $\tilde{a}$, a disjoint, closed branch of steady-state periodic trajectories, which folds back on itself at the points SN_1 and SN_3, can be found for lower values of $\tilde{s}$. The points GR_1, GR_2, and GR_3 correspond to periodic trajectories that achieve grazing incidence with the discontinuity surface $x_1 + \tilde{s} - \tilde{a} = 0$ and points of transversal intersection of the family of periodic trajectories with the discontinuity surface under variations in $\tilde{s}$.

It is again the case that each fold in the two disjoint branches of periodic trajectories is associated with a change in stability. The occurrence of two additional folds at SN_3 and SN_4 can be traced to a slightly larger value of $\tilde{a}$, at which the two branches merge at a unique point, a so-called *branch point bifurcation*. Four separate branches can be shown to emanate from this point at nonzero relative angles.

As shown in Fig. 2(c), the previous scenario is again repeated for smaller values of $\tilde{a}$. Again, the points GR_1 and GR_2 correspond to periodic trajectories that achieve grazing incidence with the discontinuity surface $x_1 + \tilde{s} - \tilde{a} = 0$. Of these, GR_1 is a point of quadratic contact of the family of periodic trajectories with the discontinuity surface under variations in $\tilde{s}$, whereas GR_2 corresponds to a point of transversal intersection of the family of periodic trajectories with the discontinuity surface under variations in $\tilde{s}$.

Here, the disjoint, closed branch of steady-state periodic trajectories has shrunk in dimension only to eventually disappear as $\tilde{a}$ is reduced further at a unique point, a so-called *isola bifurcation*. For values of $\tilde{a}$ smaller than the corresponding critical value, there exists a single branch of periodic steady-state trajectories over the entire range of intermediate and small values of $\tilde{s}$.

3. Theoretical analysis

3.1. A generalized mathematical formulation

The observations on the cantilever response made in previous sections generalize to a class of nonlinear, piecewise smooth dynamical systems in which bifurcations directly associated with the presence of discontinuities, so-called *discontinuity-induced bifurcations* (e.g., [28,30–33]), are common and necessitate mathematical analysis distinct from that of smooth systems. To this end, consider the class of hybrid dynamical systems given by a piecewise smooth vector field

$$\begin{cases} \mathbf{f}(\mathbf{x}, \boldsymbol{\mu}) & k(\mathbf{x}, \boldsymbol{\mu}) > 0 \\ \mathbf{f}(\mathbf{x}, \boldsymbol{\mu}) + k(\mathbf{x}, \boldsymbol{\mu})\,\mathbf{g}(\mathbf{x}, \boldsymbol{\mu}) & k(\mathbf{x}, \boldsymbol{\mu}) < 0 \end{cases} \tag{11}$$

for some sufficiently smooth functions $\mathbf{f}, \mathbf{g} : \mathbb{R}^n \times \mathbb{R}^m \to \mathbb{R}^n$ and $k : \mathbb{R}^n \times \mathbb{R}^m \to \mathbb{R}$. In particular, such a vector field is continuous, but not necessarily differentiable at points on the zero-level surface of k, $\{(\mathbf{x}, \boldsymbol{\mu}) \in \mathbb{R}^n \times \mathbb{R}^m \mid k(\mathbf{x}, \boldsymbol{\mu}) = 0\}$.

Suppose that, for $\boldsymbol{\mu} = \boldsymbol{\mu}_*$, there exists a periodic trajectory of this hybrid dynamical system that achieves simple tangential (grazing) contact with the zero-level surface of k at a point $\mathbf{x} = \mathbf{x}_*$ and such that $k > 0$ for all other points on the trajectory. [1] The objective of the present analysis is to predict the persistence characteristics of the grazing periodic trajectory under changes in $\boldsymbol{\mu}$ away from $\boldsymbol{\mu}_*$.

Without loss of generality, take the zero-level surface of k to be locally flat[2] at $(\mathbf{x}_*, \boldsymbol{\mu}_*)$, i.e., such that derivatives of k with respect

[1] With minor modifications to the subsequent discussion, the condition that k be positive for all other points on the trajectory can be relaxed to situations in which all other intersections with the zero-level surface of k are transversal.

[2] This can always be achieved through the use of a smooth near-identity coordinate transformation.

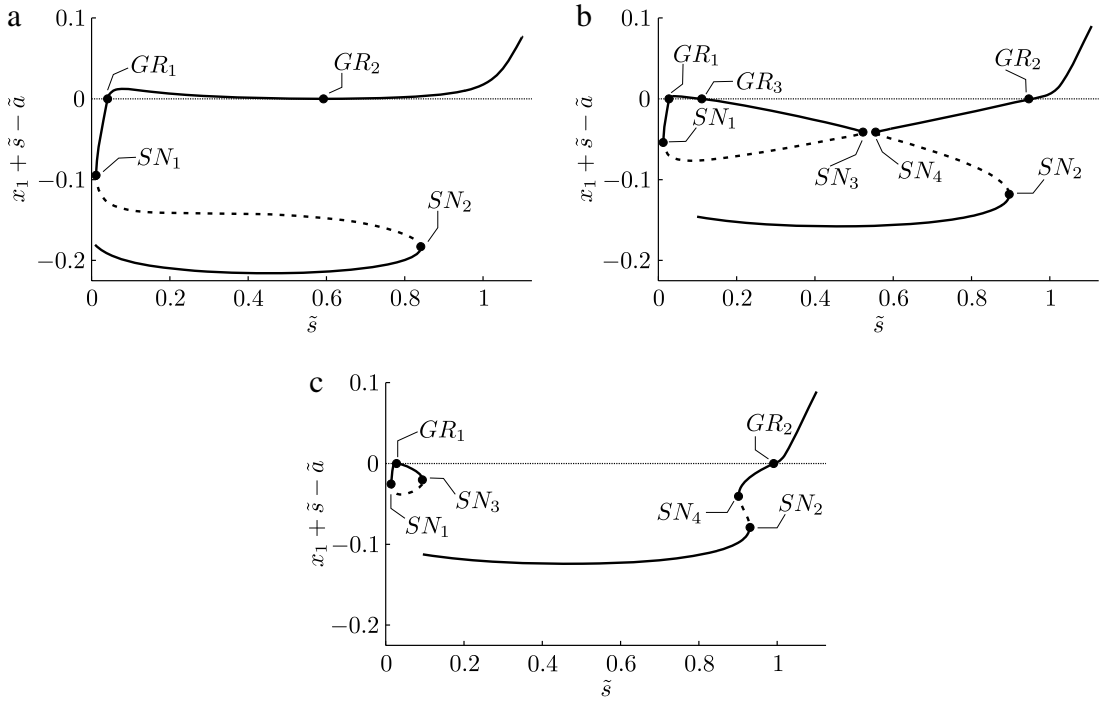

Fig. 2. Minimum values of $x_1 + \tilde{s} - \tilde{a}$ along branches of steady-state periodic trajectories under variations in $\tilde{s}$ and $\tilde{a}$ and with $\tilde{\omega} = 1$. Here, $\tilde{a} = 0.0262$ in panel (a), $\tilde{a} = 0.0171$ in panel (b), and $\tilde{a} = 0.0119$ in panel (c). Solid curves refer to branches of stable trajectories. Dashed curves refer to branches of unstable trajectories. Points denoted by GR_i refer to periodic trajectories that achieve grazing contact with the discontinuity surface $x_1 + \tilde{s} - \tilde{a} = 0$. Points denoted by SN_i refer to fold bifurcations.

to its arguments of order two or higher vanish at $(\mathbf{x}_*, \boldsymbol{\mu}_*)$. Unless otherwise noted, let the absence of arguments denote quantities evaluated at $(\mathbf{x}, \boldsymbol{\mu}) = (\mathbf{x}_*, \boldsymbol{\mu}_*)$. Simple tangential contact then implies that $\partial_{\mathbf{x}} k \cdot \mathbf{f} = 0$ and $\partial_{\mathbf{x}} h \cdot \mathbf{f} > 0$, where $h(\mathbf{x}, \boldsymbol{\mu}) = \partial_{\mathbf{x}} k(\mathbf{x}, \boldsymbol{\mu}) \cdot \mathbf{f}(\mathbf{x}, \boldsymbol{\mu})$, i.e., that the periodic trajectory intersects the zero-level surface of h transversally at the point of grazing contact with the zero-level surface of k.

Consider, for a moment, the case when $\mathbf{g} \equiv \mathbf{0}$. As shown in the Appendix, there exists a smooth map $\mathbf{P}_{h,\mathbf{f}}$ defined on a neighborhood of $(\mathbf{x}_*, \boldsymbol{\mu}_*)$, such that $\mathbf{P}_{h,\mathbf{f}}$ maps points near $\mathbf{x}_*$ onto the unique subsequent intersection with the zero-level surface of h after an elapsed time close to the period of the periodic trajectory. In particular, $\mathbf{P}_{h,\mathbf{f}}(\mathbf{x}_*, \boldsymbol{\mu}_*) = \mathbf{x}_*$, i.e., $\mathbf{x}_*$ is a fixed point of $\mathbf{P}_{h,\mathbf{f}}$ when $\boldsymbol{\mu} = \boldsymbol{\mu}_*$. Indeed, every fixed point of $\mathbf{P}_{h,\mathbf{f}}$ is associated with a periodic trajectory of the flow governed by the vector field $\mathbf{f}$. By a standard smooth analysis, the invertibility of $\mathbf{I}_n - \partial_{\mathbf{x}} \mathbf{P}_{h,\mathbf{f}}$, where $\mathbf{I}_n$ is the $n \times n$ identity matrix, implies the persistence of a locally unique branch $\boldsymbol{\xi}_{h,\mathbf{f}}(\boldsymbol{\mu})$ of fixed points of $\mathbf{P}_{h,\mathbf{f}}$ for $\boldsymbol{\mu} \approx \boldsymbol{\mu}_*$, such that $\boldsymbol{\xi}_{h,\mathbf{f}}(\boldsymbol{\mu}_*) = \mathbf{x}_*$. Indeed, for $\boldsymbol{\mu}$ sufficiently close to $\boldsymbol{\mu}_*$,

$$\pi_k(\boldsymbol{\mu}) \stackrel{\text{def}}{=} k\left(\boldsymbol{\xi}_{h,\mathbf{f}}(\boldsymbol{\mu}), \boldsymbol{\mu}\right) > 0 \tag{12}$$

implies that $k > 0$ for all other points on the corresponding periodic trajectory. In this case, $\boldsymbol{\xi}_{h,\mathbf{f}}(\boldsymbol{\mu})$ is the unique intersection of a periodic trajectory of the hybrid dynamical system with the zero-level surface of h even for nonzero functions $\mathbf{g}$. For $\pi_k(\boldsymbol{\mu}) < 0$, however, $k < 0$ on a segment of the corresponding trajectory of the flow governed by the vector field $\mathbf{f}$ and the corrections due to nonzero $\mathbf{g}$ can no longer be ignored.

Motivated by the application to the AFM cantilever, suppose that $\partial_{\mathbf{x}} k \cdot \mathbf{g} = 0$ and consider the special case of a *strong discontinuity*, such that $\varepsilon = \|\mathbf{g}\|^{-1} \ll 1$ (cf. [28]). Let $\boldsymbol{\mu} = \boldsymbol{\mu}_* + \varepsilon \Delta\boldsymbol{\mu}_1 + \varepsilon^2 \Delta\boldsymbol{\mu}_2$, where $\partial_{\boldsymbol{\mu}} \pi_k \cdot \Delta\boldsymbol{\mu}_1 = 0$ and $\partial_{\boldsymbol{\mu}} \pi_k \cdot \Delta\boldsymbol{\mu}_2 \neq 0$. Then, provided that the zero-level surface of h is locally flat at $(\mathbf{x}_*, \boldsymbol{\mu}_*)$ and

$$\partial_{\mathbf{x}} h \cdot \Delta\mathbf{x}_1 + \partial_{\boldsymbol{\mu}} h \cdot \Delta\boldsymbol{\mu}_1 = \partial_{\mathbf{x}} h \cdot \Delta\mathbf{x}_2 + \partial_{\boldsymbol{\mu}} h \cdot \Delta\boldsymbol{\mu}_2 = 0, \tag{13}$$

it follows from the Appendix that periodic trajectories of the hybrid dynamical system may be equivalently represented by solutions of

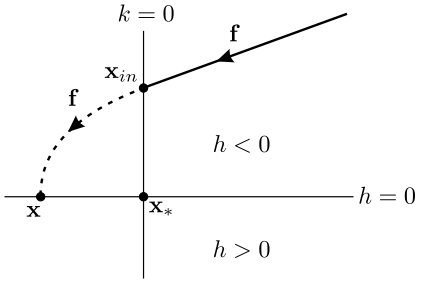

Fig. 3. For $\varepsilon \ll 1$, the point $\mathbf{x} = \mathbf{x}_* + \varepsilon\delta\mathbf{x}_1 + \varepsilon^2\delta\mathbf{x}_2$ is the forward-in-time intersection with the zero-level surface of h of the trajectory segment based at $\mathbf{x}_{in}$ on the zero-level surface of k.

the equation

$$\Delta\mathbf{x}_2 = \partial_{\mathbf{x}}\mathbf{P}_{h,\mathbf{f}} \cdot \left(\Delta\mathbf{x}_2 - \frac{4}{3}\sqrt{\frac{2}{\partial_{\mathbf{x}} h \cdot \mathbf{f}}} \left(-\partial_{\mathbf{x}} k \cdot \Delta\mathbf{x}_2 - \partial_{\boldsymbol{\mu}} k \cdot \Delta\boldsymbol{\mu}_2\right)^{3/2} \times \left(\hat{\mathbf{g}} - \frac{\partial_{\mathbf{x}} h \cdot \hat{\mathbf{g}}}{\partial_{\mathbf{x}} h \cdot \mathbf{f}} \mathbf{f} \right) \right) + \partial_{\boldsymbol{\mu}}\mathbf{P}_{h,\mathbf{f}} \cdot \Delta\boldsymbol{\mu}_2 + \frac{1}{2} \begin{pmatrix} \Delta\mathbf{x}_1^{\mathrm{T}} & \Delta\boldsymbol{\mu}_1^{\mathrm{T}} \end{pmatrix} \cdot \begin{pmatrix} \partial_{\mathbf{xx}}\mathbf{P}_{h,\mathbf{f}} & \partial_{\mathbf{x}\boldsymbol{\mu}}\mathbf{P}_{h,\mathbf{f}} \\ \partial_{\mu\mathbf{x}}\mathbf{P}_{h,\mathbf{f}} & \partial_{\boldsymbol{\mu}\boldsymbol{\mu}}\mathbf{P}_{h,\mathbf{f}} \end{pmatrix} \cdot \begin{pmatrix} \Delta\mathbf{x}_1 \\ \Delta\boldsymbol{\mu}_1 \end{pmatrix}, \tag{14}$$

where

$$\Delta\mathbf{x}_1 = \left(\mathbf{I}_n - \partial_{\mathbf{x}}\mathbf{P}_{h,\mathbf{f}}\right)^{-1} \cdot \partial_{\boldsymbol{\mu}}\mathbf{P}_{h,\mathbf{f}} \cdot \Delta\boldsymbol{\mu}_1, \tag{15}$$

and $\hat{\mathbf{g}} = \varepsilon\mathbf{g}$. In particular, let $\mathbf{x}_{in} \approx \mathbf{x}_*$ denote the intersection of the corresponding periodic trajectory with the zero-level surface of k at a point where $h < 0$. Then, $\mathbf{x} = \mathbf{x}_* + \varepsilon\Delta\mathbf{x}_1 + \varepsilon^2\Delta\mathbf{x}_2 + \mathcal{O}\left(\varepsilon^3\right)$ is the subsequent intersection with the zero-level surface of h of the trajectory segment based at $\mathbf{x}_{in}$ and governed by the vector field $\mathbf{f}$ (see Fig. 3).

Let

$$\tau = -\sqrt{-\left(\partial_{\mathbf{x}} k \cdot \Delta\mathbf{x}_2 + \partial_{\boldsymbol{\mu}} k \cdot \Delta\boldsymbol{\mu}_2\right) \frac{2}{\partial_{\mathbf{x}} h \cdot \mathbf{f}}}. \tag{16}$$

Without loss of generality, Eq. (14) can then be reduced to

$$\frac{4}{3}\alpha\tau^3 + \tau^2 + \beta = 0, \tag{17}$$

where

$$\alpha = \partial_{\mathbf{x}} k \cdot \left(\mathbf{I}_n - \partial_{\mathbf{x}}\mathbf{P}_{h,\mathbf{f}}\right)^{-1} \cdot \partial_{\mathbf{x}}\mathbf{P}_{h,\mathbf{f}} \cdot \left(\hat{\mathbf{g}} - \frac{\partial_{\mathbf{x}} h \cdot \hat{\mathbf{g}}}{\partial_{\mathbf{x}} h \cdot \mathbf{f}}\mathbf{f}\right),$$

$$\beta = \frac{2}{\partial_{\mathbf{x}} h \cdot \mathbf{f}}\left(\partial_{\boldsymbol{\mu}}\pi_k \cdot \Delta\boldsymbol{\mu}_2 + \frac{1}{2}\Delta\boldsymbol{\mu}_1^{\mathrm{T}} \cdot \partial_{\boldsymbol{\mu}}^2\pi_k \cdot \Delta\boldsymbol{\mu}_1\right), \tag{18}$$

provided that $\alpha \neq 0$. The number of negative real roots τ of this equation depends on the signs of α and β. Specifically, in the case that $\alpha > 0$, there is one negative real root for $\beta \geq 0$, two negative real roots for $-\frac{1}{12\alpha^2} \leq \beta < 0$, and no negative real roots for $\beta < -\frac{1}{12\alpha^2}$. Similarly, in the case that $\alpha < 0$, there is one negative real root for $\beta < 0$ and no negative real roots for $\beta \geq 0$ (cf. [28, 34]).

3.2. Example

The case of a harmonically excited linear oscillator with a piecewise linear, continuous stiffness affords an example of the above methodology for which closed-form expressions are available for the relevant quantities in terms of system parameters. To this end, let $\mathbf{x} \in \mathbb{R}^2 \times \mathbb{S}^1$ and consider a hybrid dynamical system of the form (11), such that

$$\mathbf{f}(\mathbf{x}, \boldsymbol{\mu}) = \begin{pmatrix} x_2 \\ -x_1 - 2\zeta x_2 + \gamma\cos x_3 \\ \omega \end{pmatrix},$$

$$\mathbf{g}(\mathbf{x}) = \pm\frac{1}{\varepsilon}\begin{pmatrix}0\\1\\0\end{pmatrix}, \quad 0 < \varepsilon \ll 1,$$

and

$$k(\mathbf{x}, \boldsymbol{\mu}) = 1 - x_1 \Rightarrow h(\mathbf{x}, \boldsymbol{\mu}) = -x_2, \tag{19}$$

where $\boldsymbol{\mu} = \begin{pmatrix}\omega & \gamma & \zeta\end{pmatrix}^{\mathrm{T}}$ denotes a vector of system parameters. Here, the sign ambiguity of $\mathbf{g}$ allows for the consideration of a hardening or softening stiffness as x_1 exceeds 1. It is straightforward to show that

$$\boldsymbol{\xi}_{h,\mathbf{f}}(\boldsymbol{\mu}) = \begin{pmatrix} \dfrac{\gamma}{\sqrt{\left(1-\omega^2\right)^2 + 4\zeta^2\omega^2}} \\ 0 \\ \arccos\dfrac{1-\omega^2}{\sqrt{\left(1-\omega^2\right)^2 + 4\zeta^2\omega^2}} \end{pmatrix} \tag{20}$$

denotes a family of fixed points of the Poincaré map $\mathbf{P}_{h,\mathbf{f}}$, such that

$$\pi_k(\boldsymbol{\mu}) = 1 - \frac{\gamma}{\sqrt{\left(1-\omega^2\right)^2 + 4\zeta^2\omega^2}}. \tag{21}$$

Given $\zeta_*, \omega_* > 0$, it now follows that

$$\begin{aligned} k(\mathbf{x}_*, \boldsymbol{\mu}_*) &= \partial_{\mathbf{x}} k(\mathbf{x}_*, \boldsymbol{\mu}_*) \cdot \mathbf{f}(\mathbf{x}_*, \boldsymbol{\mu}_*) \\ &= \partial_{\mathbf{x}} k(\mathbf{x}_*, \boldsymbol{\mu}_*) \cdot \mathbf{g}(\mathbf{x}_*, \boldsymbol{\mu}_*) = 0 \end{aligned} \tag{22}$$

and

$$\partial_{\mathbf{x}} h(\mathbf{x}_*, \boldsymbol{\mu}_*) \cdot \mathbf{f}(\mathbf{x}_*, \boldsymbol{\mu}_*) = \omega_*^2 > 0, \tag{23}$$

where

$$\boldsymbol{\mu}_* = \begin{pmatrix}\omega_* & \gamma_* = \sqrt{\left(1-\omega_*^2\right)^2 + 4\zeta_*^2\omega_*^2} & \zeta_*\end{pmatrix}^{\mathrm{T}} \tag{24}$$

and

$$\mathbf{x}_* = \boldsymbol{\xi}_{h,\mathbf{f}}(\boldsymbol{\mu}_*) = \begin{pmatrix}1 & 0 & \arccos\dfrac{1-\omega_*^2}{\gamma_*}\end{pmatrix}^{\mathrm{T}}. \tag{25}$$

To apply the analysis of the previous section, let

$$\Delta\boldsymbol{\mu}_1 = \begin{pmatrix}\Delta\omega_1 & \dfrac{2\omega_*}{\gamma_*}\left(2\omega_*\zeta_*\Delta\zeta_1 + \left(\omega_*^2 - 1 + 2\zeta_*^2\right)\Delta\omega_1\right) & \Delta\zeta_1\end{pmatrix}^{\mathrm{T}} \tag{26}$$

such that

$$\Delta\mathbf{x}_1 = \frac{4}{\gamma_*^2}\left(\zeta_*\left(1+\omega_*^2\right)\Delta\omega_1 + \omega_*\left(1-\omega_*^2\right)\Delta\zeta_1\right)\begin{pmatrix}0 & 0 & 1\end{pmatrix}^{\mathrm{T}}. \tag{27}$$

Moreover, let

$$\Delta\boldsymbol{\mu}_2 = \begin{pmatrix}\Delta\omega_2 & \Delta\gamma_2 & \Delta\zeta_2\end{pmatrix}^{\mathrm{T}}, \tag{28}$$

where $\partial_{\boldsymbol{\mu}}\pi_k \cdot \Delta\boldsymbol{\mu}_2 \neq 0$. Finally,

$$\partial_{\mathbf{x}} h(\mathbf{x}_*, \boldsymbol{\mu}_*) \cdot \Delta\mathbf{x}_2 + \partial_{\boldsymbol{\mu}} h(\mathbf{x}_*, \boldsymbol{\mu}_*) \cdot \Delta\boldsymbol{\mu}_2 = 0 \tag{29}$$

implies that

$$\Delta\mathbf{x}_2 = \begin{pmatrix}\Delta x_{21} & 0 & \Delta x_{23}\end{pmatrix} \tag{30}$$

such that

$$\tau = -\frac{1}{\omega_*}\sqrt{2\Delta x_{21}} \tag{31}$$

provided that $\Delta x_{21} > 0$.

Given $\Delta\boldsymbol{\mu}_1$ and $\Delta\boldsymbol{\mu}_2$, the number of near-grazing periodic trajectories of period $\frac{2\pi}{\omega}$ that intersect the zero-level surface of k transversally is now determined by the signs of the quantities

$$\alpha = \pm\frac{\sin\frac{2\pi\sqrt{1-\zeta_*^2}}{\omega_*}}{2\sqrt{1-\zeta_*^2}\left(\cos\frac{2\pi\sqrt{1-\zeta_*^2}}{\omega_*} - \cosh\frac{2\pi\zeta_*}{\omega_*}\right)} \tag{32}$$

and

$$\begin{aligned} \frac{\omega_*^2\gamma_*^2}{2}\beta = {} & 2\omega_*\left(\omega_*^2 - 1 + 2\zeta_*^2\right)\Delta\omega_2 - \gamma_*\Delta\gamma_2 + 4\omega_*^2\zeta_*\Delta\zeta_2 \\ & + \frac{2\zeta_*^2\left(1+3\omega_*^4\right) - \left(1-\omega_*^2\right)^3}{\gamma_*^2}\Delta\omega_1^2 \\ & + \frac{8\zeta_*\omega_*\left(1-\left(1-2\zeta_*^2\right)\omega_*^2\right)}{\gamma_*^2}\Delta\zeta_1\Delta\omega_1 \\ & + \frac{2\omega_*^2\left(1-\omega_*^2\right)^2}{\gamma_*^2}\Delta\zeta_1^2, \end{aligned} \tag{33}$$

where the $\pm$ refers back to the sign of $\mathbf{g}$. As a special case, suppose that $\Delta\zeta_1 = \Delta\omega_2 = \Delta\zeta_2 = 0$, and $\alpha > 0$. It follows that there exist one such periodic trajectory provided that

$$\Delta\gamma_2 \leq \frac{2\zeta_*^2\left(1+3\omega_*^4\right) - \left(1-\omega_*^2\right)^3}{\gamma_*^3}\Delta\omega_1^2, \tag{34}$$

two such periodic trajectories provided that

$$\Delta\gamma_2 - \frac{1}{12\alpha^2}\frac{\omega_*^2\gamma_*}{2} \leq \frac{2\zeta_*^2\left(1+3\omega_*^4\right) - \left(1-\omega_*^2\right)^3}{\gamma_*^3}\Delta\omega_1^2 < \Delta\gamma_2 \tag{35}$$

and no such periodic trajectories provided that

$$\frac{2\zeta_*^2\left(1+3\omega_*^4\right) - \left(1-\omega_*^2\right)^3}{\gamma_*^3}\Delta\omega_1^2 < \Delta\gamma_2 - \frac{1}{12\alpha^2}\frac{\omega_*^2\gamma_*}{2}. \tag{36}$$

In particular, for $\Delta\gamma_2 = \frac{1}{12\alpha^2}\frac{\omega_*^2\gamma_*}{2}$, it is evident from this analysis that $\Delta\omega_1 = 0$ corresponds to a branch point at which four branches of periodic trajectories intersect transversally when

$2\zeta_*^2\left(1+3\omega_*^4\right)-\left(1-\omega_*^2\right)^3 > 0$ and to an isolated point surrounded by closed-loop branches of periodic trajectories corresponding to smaller values of $\Delta\gamma_2$ when $2\zeta_*^2\left(1+3\omega_*^4\right)-(1-\omega_*^2)^3<0$.

A numerical example is afforded by the parameter choices $\varepsilon = 0.1$, $\omega_* = 0.52$, and $\zeta_* = 0.04$ and with positive stiffness of the spring represented by $\mathbf{g}$, from which it follows that $\alpha \approx 0.99$ and $2\zeta_*^2\left(1+3\omega_*^4\right)-\left(1-\omega_*^2\right)^3 \approx -0.38$. Fig. 4(a) and (b) show a comparison between solution branches obtained using numerical continuation and those obtained directly from the perturbation analysis. In this case, $\Delta\gamma_2 \approx 0.0086$ for the isolated point at the center of the family of concentric solution branches, whereas $\frac{1}{12\alpha^2}\frac{\omega_*^2\gamma_*}{2} \approx 0.0083$. Fig. 4(c) and (d) show a similar comparison in the case with $\varepsilon = 0.1$, $\omega_* = 1.2$, and $\zeta_* = 0.04$ and positive stiffness, from which it follows that $\alpha \approx 0.83$ and $2\zeta_*^2\left(1+3\omega_*^4\right)-\left(1-\omega_*^2\right)^3 \approx 0.11$. In this case, $\Delta\gamma_2 \approx 0.041$ for the branch point at the intersection of the solution branches, whereas $\frac{1}{12\alpha^2}\frac{\omega_*^2\gamma_*}{2} \approx 0.040$.

In contrast, suppose that $\Delta\zeta_1 = \Delta\omega_2 = \Delta\zeta_2 = 0$, and $\alpha < 0$. It follows that there exist one such periodic trajectory provided that

$$\frac{2\zeta_*^2\left(1+3\omega_*^4\right)-\left(1-\omega_*^2\right)^3}{\gamma_*^3}\Delta\omega_1^2 < \Delta\gamma_2 \tag{37}$$

and no such periodic trajectories provided that

$$\Delta\gamma_2 \le \frac{2\zeta_*^2\left(1+3\omega_*^4\right)-\left(1-\omega_*^2\right)^3}{\gamma_*^3}\Delta\omega_1^2. \tag{38}$$

In the case that $\Delta\boldsymbol{\mu}_1 = \mathbf{0}$, the analysis in the Appendix reduces to a known formulation, originally derived in [28] (see also [32]). In this case, it follows from the general expression in (18) and the specific formula in (33) that β varies monotonically with $\partial_{\boldsymbol{\mu}}\pi_k \cdot \Delta\boldsymbol{\mu}_2$. It is, consequently, not possible to capture the branch point and isola bifurcation structure shown above without the consideration of nonzero $\Delta\boldsymbol{\mu}_1$, thus justifying the need for the extension developed in the Appendix.

4. Qualitative analysis

4.1. The strength of the discontinuity

In an actual application of the perturbation analysis undertaken in the previous section, it is inevitably necessary to forego the reliance on the $\mathcal{O}$ notation and to substitute for ε a numerical value consistent with the physical model. This raises the specter of higher-order terms omitted from the analysis and their effects on the near-grazing bifurcation behavior. Indeed, without the assumption of a *strong discontinuity*, it is not possible to rigorously establish a nontrivial contribution from the function $\mathbf{g}(\mathbf{x},\boldsymbol{\mu})$ that relies on a truncated expansion of the composite mapping to $\mathcal{O}\left(\varepsilon^2\right)$ as was done in the Appendix.

While the results in Section 3 can be expected to apply with increased accuracy as $\varepsilon \to 0$, it is naturally difficult to determine whether a given numerical value for ε is indeed small enough. Thus, in spite of the suggestive similarity between the characteristic bifurcation diagrams found in the previous section and those obtained using numerical continuation in the case of the atomic-force-microscopy model, some care must be taken in establishing the applicability of the perturbation method in the latter case.

As shown in Section 2, the response of the atomic-force-microscope cantilever is described by a vector field of the form (11), such that

$$\mathbf{f}(\mathbf{x},\boldsymbol{\mu}) = \begin{pmatrix} x_2 \\ -Q^{-1}x_2 - x_1 + \sqrt{\left(1-\tilde{\omega}^2\right)^2 + Q^{-2}\tilde{\omega}^2}\cos x_3 - \dfrac{\sigma_a\tilde{a}^3}{\left(x_1+\tilde{s}\right)^2} \\ \tilde{\omega} \end{pmatrix}, \tag{39}$$

$$\mathbf{g}(\mathbf{x},\boldsymbol{\mu}) = \begin{pmatrix} 0 \\ -\sigma_a\tilde{a}\dfrac{x_1+\tilde{s}+\tilde{a}}{\left(x_1+\tilde{s}\right)^2} - \dfrac{\sigma_r}{\sqrt{\tilde{a}}}\sqrt{\tilde{a}-x_1-\tilde{s}} \\ 0 \end{pmatrix} \tag{40}$$

and

$$k(\mathbf{x},\boldsymbol{\mu}) = x_1 + \tilde{s} - \tilde{a} \Rightarrow h(\mathbf{x},\boldsymbol{\mu}) = x_2, \tag{41}$$

where $\boldsymbol{\mu} = \begin{pmatrix}\tilde{s} & \tilde{a} & \tilde{\omega}\end{pmatrix}^{\mathrm{T}}$ denotes a vector of system parameters and

$$\sigma_a = \frac{HR}{6m\omega_0^2a^3}, \qquad \sigma_r = \frac{4}{3}\frac{E^*\sqrt{Ra}}{m\omega_0^2} \tag{42}$$

for some set of fixed numerical quantities, H, R, E^*, $m\omega_0^2$, the quality factor Q, and a given in Table 1. In particular, choose $\mathbf{x}_*$ and $\boldsymbol{\mu}_*$ such that $x_{1*} + \tilde{s}_* = \tilde{a}_*$. Then

$$\|\mathbf{g}(\mathbf{x}_*,\boldsymbol{\mu}_*)\| = 2\sigma_a \approx 1 \tag{43}$$

is independent of the repulsive contact force but captures the discontinuity in the attractive terms.

Although the value of $\|\mathbf{g}(\mathbf{x}_*,\boldsymbol{\mu}_*)\|$ is independent of $\boldsymbol{\mu}_*$, the degree to which its magnitude suffices to argue for the negligible contribution of higher-order terms in ε must be evaluated on a case-by-case basis. As an example, for the parameter vector $\boldsymbol{\mu}_* \approx \begin{pmatrix}0.5926 & 0.0262 & 1\end{pmatrix}^{\mathrm{T}}$ corresponding to the point labeled as GR_2 in Fig. 2(a) and for which $\mathbf{x}_* \approx \begin{pmatrix}-0.5664 & 0 & 5.6811\end{pmatrix}^{\mathrm{T}}$,

$$\varepsilon \sim \frac{|\partial_{\mathbf{x}}h\cdot\mathbf{f}|}{|\partial_{\mathbf{x}}h\cdot\mathbf{g}|} \approx 0.5. \tag{44}$$

In contrast, for the parameter vector $\boldsymbol{\mu}_* \approx \begin{pmatrix}0.0262 & 0.0119 & 1\end{pmatrix}^{\mathrm{T}}$ corresponding to the point labeled as GR_1 in Fig. 2(c) and for which $\mathbf{x}_* \approx \begin{pmatrix}-0.0144 & 0 & 6.2710\end{pmatrix}^{\mathrm{T}}$,

$$\varepsilon \sim \frac{|\partial_{\mathbf{x}}h\cdot\mathbf{f}|}{|\partial_{\mathbf{x}}h\cdot\mathbf{g}|} \approx 0.01. \tag{45}$$

Thus, $\mathbf{g}$ certainly appears to qualify as a strong discontinuity in the latter case, whereas this label is more questionable in the former case.

A further complication arises from the size of the quantity α in Eq. (18), since the location of the fold point corresponding to $\beta = -\frac{1}{12\alpha^2}$ occurs at $\tau = -\frac{1}{2\alpha}$. Since the analysis presupposes that τ is $\mathcal{O}(1)$ as compared to ε, its applicability in accurately predicting the existence of branch point and isola bifurcations is compromised in the case of small α. Here, $\alpha \approx 1.3909$ for the parameter vector $\boldsymbol{\mu}_* \approx \begin{pmatrix}0.5926 & 0.0262 & 1\end{pmatrix}^{\mathrm{T}}$ and $\alpha \approx 0.0087$ for the parameter vector $\boldsymbol{\mu}_* \approx \begin{pmatrix}0.0262 & 0.0119 & 1\end{pmatrix}^{\mathrm{T}}$. Thus, even though $\mathbf{g}$ satisfies the conditions for a strong discontinuity in the latter case, the small value of α again raises the possibility of a significant influence from higher-order terms neglected in the perturbation analysis.

4.2. Discontinuities in the attractive and repulsive terms

That the discontinuity in the attractive component of the tip–sample interaction force alone is unable to explain the branch point and isola bifurcations alluded to in the discussion of Fig. 2 is further evident by a similar numerical analysis performed with σ_r temporarily set to 0. In this case, as seen in Fig. 5, there are no

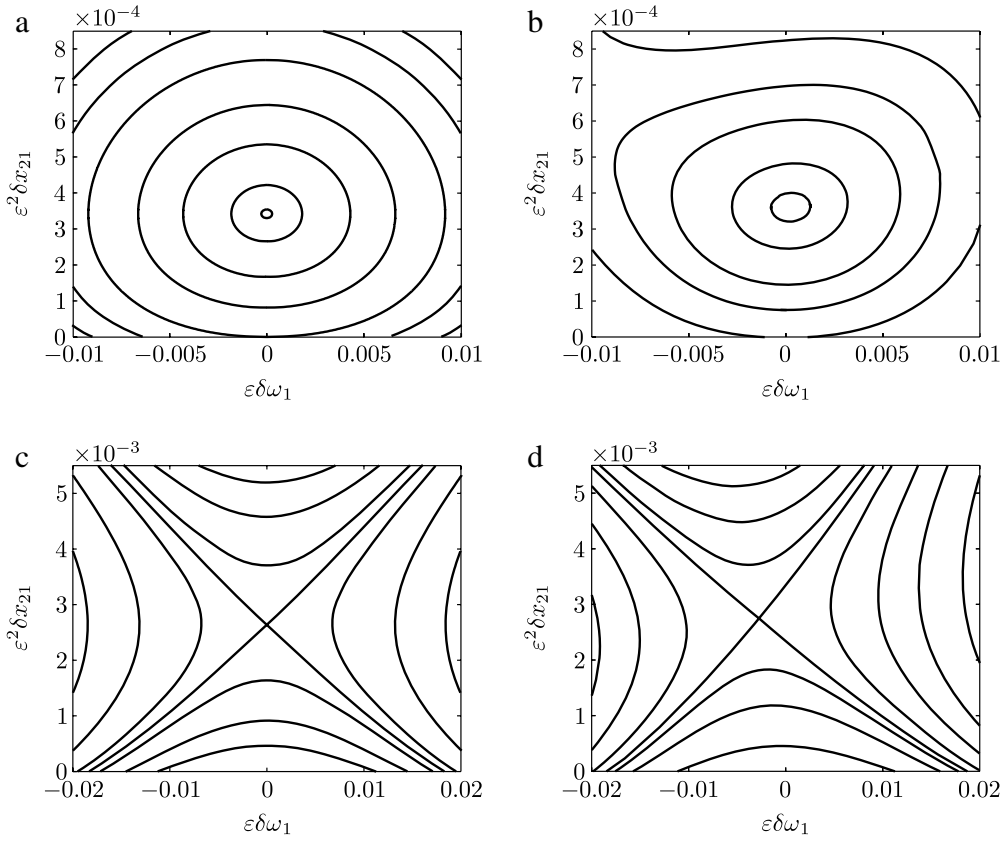

Fig. 4. Comparison between solution branches obtained using the perturbation analysis (left panels) and numerical continuation (right panels). In (a) and (b), $\varepsilon = 0.1$, $\omega_* = 0.52$, $\zeta_* = 0.04$. In (c) and (d), $\varepsilon = 0.1$, $\omega_* = 1.2$, $\zeta_* = 0.04$. In both cases, the discontinuity corresponds to a hardening stiffness.

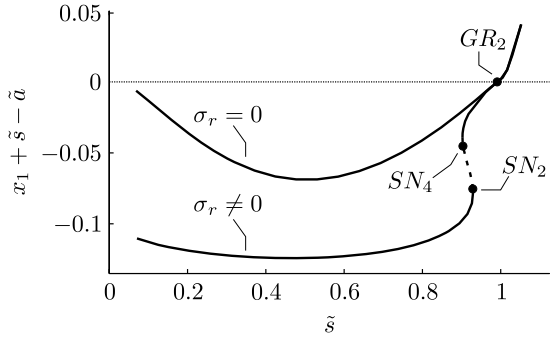

Fig. 5. Minimum values of $x_1 + \tilde{s} - \tilde{a}$ along branches of steady-state periodic trajectories under variations in $\tilde{s}$ for $\tilde{a} = 0.0119$ and $\tilde{\omega} = 1$ with $\sigma_r = 0$ and with σ_r equal to the value in Table 1. Notation is identical to that used in Fig. 2.

longer any folds in the branch of steady-state periodic trajectories. The onset of the repulsive terms in the tip–sample interaction force is thus essential (at least for the parameter values used here) to generate the bifurcation structure observed previously.

To explore the necessity of the repulsive terms further, Fig. 6 contrasts variations in the real and imaginary parts of the two nontrivial Floquet multipliers corresponding to the periodic steady-state trajectories for decreasing values of $\tilde{a}$ away from the points GR_2 in Fig. 2(a) and GR_1 in Fig. 2(c) with the original value of σ_r (solid) to those found in the case when $\sigma_r = 0$ (dashed). In both cases, there is an initial rapid growth in the deviation of the Floquet multipliers for near-grazing trajectories from the values found for the grazing trajectory. This is consistent with the perturbation analysis, which predicts lowest-order variations proportional to $\sqrt{-\beta}$. In the case that $\sigma_r = 0$ the Floquet multipliers get close to, but fail to cross the unit circle. In contrast, with the original value of σ_r, the contribution from the onset of the repulsive force interactions tips the scale in favor of a bifurcation and the associated fold in the branch of periodic steady-state trajectories.

To establish whether the discontinuity in the repulsive tip–sample interaction force indeed is sufficient to generate the observed bifurcation behavior, we consider replacing $\mathbf{g}$ with the vector field

$$\tilde{\mathbf{g}}(\mathbf{x}, \boldsymbol{\mu}) = \begin{pmatrix} 0 \\ \sigma_a \dfrac{\left(2x_1 + 2\tilde{s} + \tilde{a}\right)\left(x_1 + \tilde{s} - \tilde{a}\right)}{\left(x_1 + \tilde{s}\right)^2} - \dfrac{\sigma_r}{\sqrt{\tilde{a}}}\sqrt{\tilde{a} - x_1 - \tilde{s}} \\ 0 \end{pmatrix}, \quad (46)$$

for which $\tilde{\mathbf{g}}(\mathbf{x}_*, \boldsymbol{\mu}_*) = \mathbf{0}$. The corresponding variations in the real and imaginary parts of the two nontrivial Floquet multipliers shown in Fig. 7 clearly disagree with the near-grazing observations made using the original vector field. Indeed, although a saddle–node bifurcation again occurs at values of $x_1 + \tilde{s} - \tilde{a}$ of the same order of magnitude as in Fig. 6, the corresponding value of $\tilde{a} \approx 10^{-4}$ is far outside the near-grazing region. The discontinuity in the attractive tip–sample interaction force is thus clearly essential (at least for the parameter values used here) to generate the near-grazing bifurcation structure.

5. Discussion

The analysis in the previous sections has put forward a plausible explanation for the occurrence of branch point and isola bifurcations in the near-grazing dynamics during tapping-mode atomic-force microscopy in the vicinity of critical parameter values

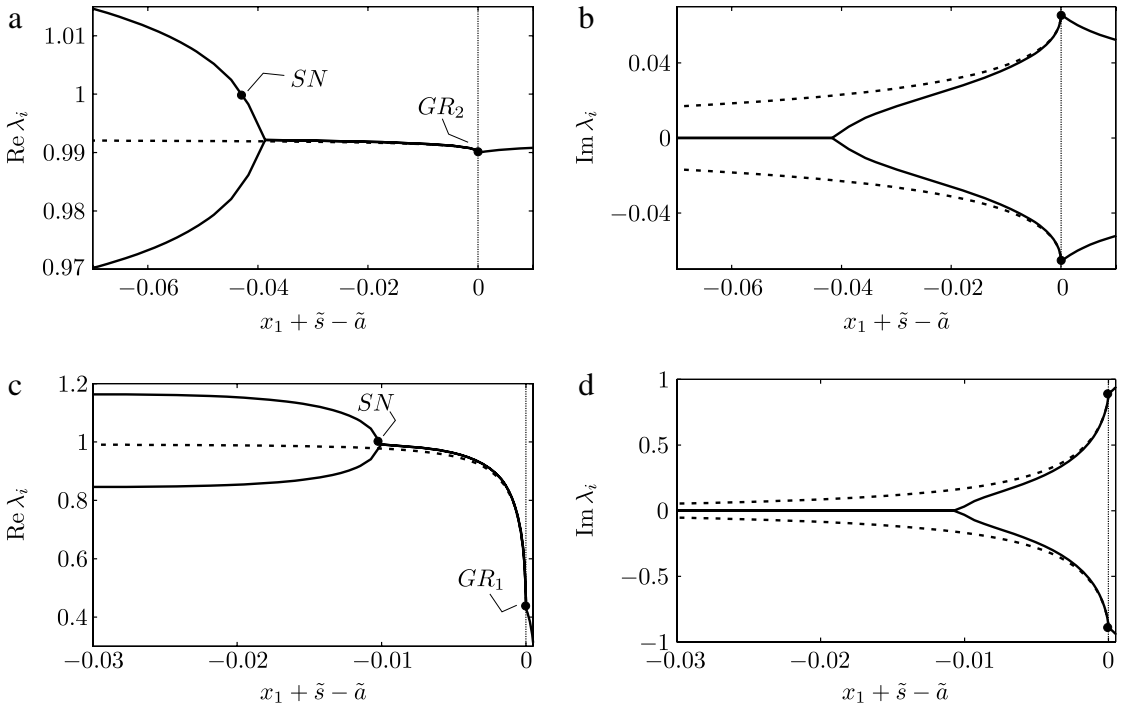

Fig. 6. Variations in real (left panels) and imaginary (right panels) parts of nontrivial Floquet multipliers under variations in $\tilde{a}$. Here, GR_2 refers to the corresponding point in Fig. 2(a) and GR_1 refers to the corresponding point in Fig. 2(c). Solid curves refer to the case that σ_r equals the value given in Table 1. Dashed curves refer to the case that $\sigma_r = 0$. The fold bifurcations denoted by *SN* occur at $\tilde{a} \approx 0.0171$ in the case of the top panels and at $\tilde{a} \approx 0.0094$ in the case of the bottom panels, i.e., in the near-grazing regime.

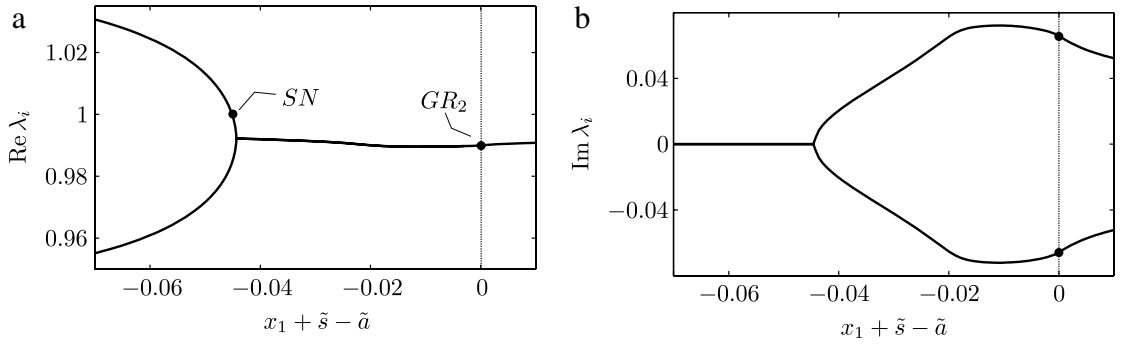

Fig. 7. Variations in real (left panel) and imaginary (right panel) parts of nontrivial Floquet multipliers under variations in $\tilde{a}$ with $\tilde{\mathbf{g}}$ replacing $\mathbf{g}$. Here, GR_2 refers to the corresponding point in Fig. 2(a). The fold bifurcation denoted by *SN* occurs at $\tilde{a} \approx 0.0001$, i.e., far outside of the near-grazing region.

associated with degenerate grazing periodic trajectories. In particular, in the case of "strong" discontinuities, the discontinuity-mapping-based theory has established the generic nature of such bifurcation scenarios in arbitrary piecewise smooth dynamical systems. The challenge of applying the theory in a quantitative example has further illustrated the methodology as well as the characteristic near-grazing variations in Floquet multipliers predicted by the theory and documented in previously published work. Indeed, the agreement between the theory and the actual system response would be expected to be further improved for alternate models of the tip–sample interaction force (e.g., [21]), for which the strength of the discontinuity is at least an order of magnitude larger, even near points corresponding to GR_2 in Fig. 2(a).

The dynamical model employed here to investigate the cantilever dynamics has been purposely chosen to agree with that used by García and San Paulo [10] (and a number of other authors). The reduction of the deformation dynamics of the cantilever to a single mechanical mode may in many instances of practical importance fall far short of an acceptable quantitative accuracy in approximating the actual cantilever response (cf. [35,36]). On the other hand, the qualitative features exhibited by this model appear substantiated by experimental results. Moreover, the discontinuity-induced phenomenology clearly generalizes to arbitrary state-space dimensions, as established by the theoretical analysis in Section 3 and the Appendix. Thus, whereas a more accurate quantitative description of the cantilever response would warrant the inclusion of more than a single mechanical mode, the objective of the paper is still met with the present discussion.

The choice of a harmonically excited dither piezo agrees with a typical implementation in existing intermittent-contact-mode atomic-force-microscope hardware. For the recently proposed multi-frequency excitation schemes, the cantilever response would typically involve at least one incommensurable pair of frequencies, corresponding to a quasiperiodic steady-state trajectory. Although the discontinuity-mapping technique can be generalized to this situation [37,38], the practical implementation as well as the predicted consequences of grazing differ in substantial ways from that presented here. The results presented here would apply

with appropriately computed numerical values as long as the cantilever response at grazing is periodic. Thus, it is not necessary that the excitation be harmonic. In fact, a periodic cantilever response is also possible by using a nonlinear feedback strategy to control the dither excitation (see recent work by Yabuno et al. [39]).

Finally, the present discussion has relied on the existence of a discontinuity surface in state space along which the vector field is continuous with a discontinuous first derivative. The theory would therefore not be a priori applicable to smooth formulations, for example those based on a Lennard–Jones-type tip–sample interaction force (e.g., [20]). However, as argued in [24] traces of the bifurcation behavior observed in the case of discontinuous vector fields should still be evident in the case of a vector field with a localized rapid variability in its derivative. It would again be necessary to use some judgment in evaluating the extent to which an observed bifurcation was directly related to such a "soft" discontinuity, much in the same way as achieved in the previous section.

It is certainly conceivable that the presence of the codimension-two branch point and isola bifurcations in a given piecewise smooth dynamical system might be desirable in a given practical example. In the case of the atomic-force microscope, however, operation at parameter values close to the those corresponding to degenerate grazing makes the cantilever response sensitive to sudden, unanticipated transitions between steady-state trajectories. The emergence of a gap in the branch of low-amplitude oscillations further places limits on the operating point in cases where low-amplitude oscillations are the preferred choice for imaging soft materials.

In addition to passive avoidance of the parameter regions corresponding to the degenerate bifurcations and gap formation, feedback strategies could be envisioned that would modify the effective value of α guaranteeing a unique near-grazing branch of periodic steady-state trajectories. Such strategies have been successfully formulated in the case of impact oscillators (where the lowest-order terms in the composition $\mathbf{P}_{h,\mathbf{f}} \circ \mathbf{D}_{\mathbf{f},\mathbf{g}}$ derived in the Appendix are of square-root order) in [40–42] and, more recently, in the case of impact oscillators in the presence of dry friction [43]. A candidate strategy for the piecewise smooth case has recently been uncovered by the authors and will be documented in a separate publication.

Acknowledgments

This work was supported by National Science Foundation CMMI Grant Nos. 0510044 and 0619028, a GOALI project performed in collaboration with Veeco Metrology, LLC.

Appendix

A.1. Preliminaries

Given a sufficiently smooth vector field $\mathbf{f} : \mathbb{R}^n \to \mathbb{R}^n$ denote by $\mathbf{\Phi}_\mathbf{f} : \mathbb{R}^n \times \mathbb{R} \to \mathbb{R}^n$ the corresponding flow function, such that

$$\partial_t \mathbf{\Phi}_\mathbf{f}(\mathbf{x}, t) = \mathbf{f}(\mathbf{\Phi}_\mathbf{f}(\mathbf{x}, t)), \qquad \mathbf{\Phi}_\mathbf{f}(\mathbf{x}, 0) = \mathbf{x}. \tag{47}$$

Derivatives of $\mathbf{\Phi}_\mathbf{f}$ with respect to t and/or $\mathbf{x}$ may be obtained inductively from this defining initial-value problem.

Now suppose that there exist $\mathbf{x}^*$ and t^*, such that $h(\mathbf{\Phi}_\mathbf{f}(\mathbf{x}^*, t^*)) = 0$ and

$$\partial_\mathbf{x} h\left(\mathbf{\Phi}_\mathbf{f}\left(\mathbf{x}^*, t^*\right)\right) \cdot \mathbf{f}\left(\mathbf{\Phi}_\mathbf{f}\left(\mathbf{x}^*, t^*\right)\right) > 0 \tag{48}$$

for some sufficiently smooth field $h : \mathbb{R}^n \to \mathbb{R}$. It follows from the implicit function theorem that there exists a locally unique smooth function $\tau_{h,\mathbf{f}}(\mathbf{x})$, such that $\tau_{h,\mathbf{f}}(\mathbf{x}^*) = t^*$ and

$$h\left(\mathbf{\Phi}_\mathbf{f}\left(\mathbf{x}, \tau_{h,\mathbf{f}}(\mathbf{x})\right)\right) = 0 \tag{49}$$

for $\mathbf{x} \approx \mathbf{x}^*$. Derivatives of $\tau_{h,\mathbf{f}}$ with respect to $\mathbf{x}$ evaluated at $\mathbf{x}^*$ may then be obtained through implicit differentiation. In this case, let

$$\mathbf{P}_{h,\mathbf{f}}(\mathbf{x}) = \mathbf{\Phi}_\mathbf{f}\left(\mathbf{x}, \tau_{h,\mathbf{f}}(\mathbf{x})\right) \tag{50}$$

denote the projection along flow trajectories onto $h = 0$. Derivatives of $\mathbf{P}_{h,\mathbf{f}}$ with respect to $\mathbf{x}$ evaluated at $\mathbf{x}^*$ are then obtained by the use of the chain rule. In particular, $\mathbf{P}_{h,\mathbf{f}}$ may be expanded in a Taylor expansion in $\mathbf{x} - \mathbf{x}^*$ for $\mathbf{x} \approx \mathbf{x}^*$.

A.2. A discontinuity mapping

Consider the hybrid dynamical system corresponding to the piecewise smooth vector field

$$\begin{cases} \mathbf{f}(\mathbf{x}) & k(\mathbf{x}) > 0 \\ \mathbf{f}(\mathbf{x}) + k(\mathbf{x})\,\mathbf{g}(\mathbf{x}) & k(\mathbf{x}) < 0 \end{cases} \tag{51}$$

for some sufficiently smooth fields $\mathbf{f}, \mathbf{g} : \mathbb{R}^n \to \mathbb{R}^n$ and $k : \mathbb{R}^n \to \mathbb{R}$, where, without loss of generality, $k(\mathbf{0}) = 0$ and $k = 0$ is locally flat at $\mathbf{x} = \mathbf{0}$.

Unless otherwise noted, let the absence of an argument denote the value of a function at $\mathbf{x} = \mathbf{0}$ and suppose that $\partial_\mathbf{x} k \cdot \mathbf{f} = \partial_\mathbf{x} k \cdot \mathbf{g} = 0$ and $\partial_\mathbf{x} k \cdot \partial_\mathbf{x}\mathbf{f} \cdot \mathbf{f} > 0$. Let $h(\mathbf{x}) = \partial_\mathbf{x} k(\mathbf{x}) \cdot \mathbf{f}(\mathbf{x})$, such that $\partial_\mathbf{x} k \cdot \partial_\mathbf{x}\mathbf{f} \cdot \mathbf{f} = \partial_\mathbf{x} h \cdot \mathbf{f}$ and denote by $\mathbf{D}_{\mathbf{f},\mathbf{g}}$ the *discontinuity mapping* defined on a neighborhood of $\mathbf{0}$ on $h = 0$, such that $\mathbf{D}_{\mathbf{f},\mathbf{g}}(\mathbf{x})$ equals the identity provided that $k(\mathbf{x}) > 0$ and results from the composition of a trajectory segment of $\mathbf{\Phi}_\mathbf{f}$ from $\mathbf{x}$ backward in time to $k = 0$, followed by a trajectory segment of $\mathbf{\Phi}_{\mathbf{f}+k\mathbf{g}}$ forward in time to $k = 0$, and followed by a trajectory segment of $\mathbf{\Phi}_\mathbf{f}$ backward in time to $h = 0$ provided that $k(\mathbf{x}) < 0$.

As a special case, suppose that $\varepsilon = \|\mathbf{g}\|^{-1} \ll 1$. Then, provided that $\partial_\mathbf{x} k \cdot \Delta\mathbf{x}_1 = 0$, it follows that

$$\begin{aligned} \mathbf{\Phi}_\mathbf{f}\left(\varepsilon\Delta\mathbf{x}_1 + \varepsilon^2\Delta\mathbf{x}_2, \varepsilon\tau\right) &= \varepsilon\left(\Delta\mathbf{x}_1 + \tau\mathbf{f}\right) \\ &+\varepsilon^2\left(\Delta\mathbf{x}_2 + \tau\,\partial_\mathbf{x}\mathbf{f} \cdot \Delta\mathbf{x}_1 + \frac{\tau^2}{2}\partial_\mathbf{x}\mathbf{f} \cdot \mathbf{f}\right) + \mathcal{O}\left(\varepsilon^3\right) \end{aligned} \tag{52}$$

and

$$\begin{aligned} \mathbf{\Phi}_{\mathbf{f}+k\mathbf{g}}\left(\varepsilon\Delta\mathbf{x}_1 + \varepsilon^2\Delta\mathbf{x}_2, \varepsilon\tau\right) &= \mathbf{\Phi}_\mathbf{f}\left(\varepsilon\Delta\mathbf{x}_1 + \varepsilon^2\Delta\mathbf{x}_2, \varepsilon\tau\right) \\ &+\varepsilon^2\tau\hat{\mathbf{g}}\left(\partial_\mathbf{x} k \cdot \Delta\mathbf{x}_2 + \frac{\tau}{2}\partial_\mathbf{x} k \cdot \partial_\mathbf{x}\mathbf{f} \cdot \Delta\mathbf{x}_1 + \frac{\tau^2}{6}\partial_\mathbf{x} h \cdot \mathbf{f}\right) \\ &+\mathcal{O}\left(\varepsilon^3\right), \end{aligned} \tag{53}$$

where $\hat{\mathbf{g}} = \varepsilon\mathbf{g}$. In particular, provided that $h(\mathbf{x}) = 0$ is locally flat at $\mathbf{x} = \mathbf{0}$, $\partial_\mathbf{x} h \cdot \Delta\mathbf{x}_1 = \partial_\mathbf{x} h \cdot \Delta\mathbf{x}_2 = 0$, and $\partial_\mathbf{x} k \cdot \Delta\mathbf{x}_2 < 0$, it follows that

$$\begin{aligned} \mathbf{D}_{\mathbf{f},\mathbf{g}}\left(\varepsilon\Delta\mathbf{x}_1 + \varepsilon^2\Delta\mathbf{x}_2\right) &= \varepsilon\Delta\mathbf{x}_1 \\ &+\varepsilon^2\left(\Delta\mathbf{x}_2 - \frac{4}{3}\sqrt{\frac{2}{\partial_\mathbf{x} h \cdot \mathbf{f}}}\left(-\partial_\mathbf{x} k \cdot \Delta\mathbf{x}_2\right)^{3/2}\left(\hat{\mathbf{g}} - \frac{\partial_\mathbf{x} h \cdot \hat{\mathbf{g}}}{\partial_\mathbf{x} h \cdot \mathbf{f}}\mathbf{f}\right)\right) \\ &+\mathcal{O}\left(\varepsilon^3\right). \end{aligned} \tag{54}$$

This formula reduces to the result in [28] provided that $\Delta\mathbf{x}_1 = \mathbf{0}$. To the best of our knowledge, the generalization to the case of $\Delta\mathbf{x}_1 \neq \mathbf{0}$ and orthogonal to $\partial_\mathbf{x} k$ and $\partial_\mathbf{x} h$ is original to this paper. In particular, in this case, the formula establishes the absence of a contribution from $\Delta\mathbf{x}_1$ at $\mathcal{O}\left(\varepsilon^2\right)$.

A.3. Fixed points

Without loss of generality, let $\mathbf{x} \mapsto \begin{pmatrix}\mathbf{x} & \boldsymbol{\mu}\end{pmatrix}^\mathrm{T}$ for some vector $\boldsymbol{\mu} \in \mathbb{R}^m$ of system parameters corresponding to the replacements $\mathbf{f}(\mathbf{x}) \mapsto \begin{pmatrix}\mathbf{f}(\mathbf{x}, \boldsymbol{\mu}) & \mathbf{0}_m\end{pmatrix}^\mathrm{T}$, $\mathbf{g}(\mathbf{x}) \mapsto \begin{pmatrix}\mathbf{g}(\mathbf{x}, \boldsymbol{\mu}) & \mathbf{0}_m\end{pmatrix}^\mathrm{T}$, $\mathbf{P}_{h,\mathbf{f}}(\mathbf{x}) \mapsto \begin{pmatrix}\mathbf{P}_{h,\mathbf{f}}(\mathbf{x}, \boldsymbol{\mu}) & \boldsymbol{\mu}\end{pmatrix}^\mathrm{T}$, and $\mathbf{D}_{\mathbf{f},\mathbf{g}}(\mathbf{x}) \mapsto \begin{pmatrix}\mathbf{D}_{\mathbf{f},\mathbf{g}}(\mathbf{x}, \boldsymbol{\mu}) & \boldsymbol{\mu}\end{pmatrix}^\mathrm{T}$, where $\mathbf{0}_m$ is the zero vector in $\mathbb{R}^m$. Suppose that $\mathbf{P}_{h,\mathbf{f}}(\mathbf{0}, \mathbf{0}) = \mathbf{0}$ and $\mathbf{I}_n - \partial_\mathbf{x}\mathbf{P}_{h,\mathbf{f}}$

$$\mathbf{P}_{h,\mathbf{f}}\left(\mathbf{D}_{\mathbf{f},\mathbf{g}}\left(\varepsilon\Delta\mathbf{x}_1+\varepsilon^2\Delta\mathbf{x}_2,\varepsilon\Delta\boldsymbol{\mu}_1+\varepsilon^2\Delta\boldsymbol{\mu}_2\right),\varepsilon\Delta\boldsymbol{\mu}_1+\varepsilon^2\Delta\boldsymbol{\mu}_2\right)=\varepsilon\left(\partial_{\mathbf{x}}\mathbf{P}_{h,\mathbf{f}}\cdot\Delta\mathbf{x}_1+\partial_{\boldsymbol{\mu}}\mathbf{P}_{h,\mathbf{f}}\cdot\Delta\boldsymbol{\mu}_1\right)$$
$$+\varepsilon^2\left(\begin{array}{c}\partial_{\mathbf{x}}\mathbf{P}_{h,\mathbf{f}}\cdot\left(\Delta\mathbf{x}_2-\dfrac{4}{3}\sqrt{\dfrac{2}{\partial_{\mathbf{x}}h\cdot\mathbf{f}}}\left(-\partial_{\mathbf{x}}k\cdot\Delta\mathbf{x}_2-\partial_{\boldsymbol{\mu}}k\cdot\Delta\boldsymbol{\mu}_2\right)^{3/2}\left(\hat{\mathbf{g}}-\dfrac{\partial_{\mathbf{x}}h\cdot\hat{\mathbf{g}}}{\partial_{\mathbf{x}}h\cdot\mathbf{f}}\mathbf{f}\right)\right)\right)\\ +\partial_{\boldsymbol{\mu}}\mathbf{P}_{h,\mathbf{f}}\cdot\Delta\boldsymbol{\mu}_2+\dfrac{1}{2}\begin{pmatrix}\Delta\mathbf{x}_1^{\mathrm{T}} & \Delta\boldsymbol{\mu}_1^{\mathrm{T}}\end{pmatrix}\cdot\begin{pmatrix}\partial_{\mathbf{xx}}\mathbf{P}_{h,\mathbf{f}} & \partial_{\mathbf{x}\boldsymbol{\mu}}\mathbf{P}_{h,\mathbf{f}}\\ \partial_{\boldsymbol{\mu}\mathbf{x}}\mathbf{P}_{h,\mathbf{f}} & \partial_{\boldsymbol{\mu}\boldsymbol{\mu}}\mathbf{P}_{h,\mathbf{f}}\end{pmatrix}\cdot\begin{pmatrix}\Delta\mathbf{x}_1\\ \Delta\boldsymbol{\mu}_1\end{pmatrix}\end{array}\right)+\mathcal{O}\left(\varepsilon^3\right)$$

Box I.

$$\mathbf{P}_{h,\mathbf{f}}\left(\mathbf{D}_{\mathbf{f},\mathbf{g}}\left(\varepsilon^2\Delta\mathbf{x}_2,\varepsilon^2\Delta\boldsymbol{\mu}_2\right),\varepsilon^2\Delta\boldsymbol{\mu}_2\right)=\varepsilon^2\left(\begin{array}{c}\partial_{\mathbf{x}}\mathbf{P}_{h,\mathbf{f}}\cdot\left(\Delta\mathbf{x}_2-\dfrac{4}{3}\sqrt{\dfrac{2}{\partial_{\mathbf{x}}h\cdot\mathbf{f}}}\left(-\partial_{\mathbf{x}}k\cdot\Delta\mathbf{x}_2-\partial_{\boldsymbol{\mu}}k\cdot\Delta\boldsymbol{\mu}_2\right)^{3/2}\left(\hat{\mathbf{g}}-\dfrac{\partial_{\mathbf{x}}h\cdot\hat{\mathbf{g}}}{\partial_{\mathbf{x}}h\cdot\mathbf{f}}\mathbf{f}\right)\right)\right)\\ +\partial_{\boldsymbol{\mu}}\mathbf{P}_{h,\mathbf{f}}\cdot\Delta\boldsymbol{\mu}_2\end{array}\right)+\mathcal{O}\left(\varepsilon^3\right)$$

Box II.

is invertible, where $\mathbf{I}_n$ is the $n\times n$ identity matrix. It follows from the implicit function theorem that there exists a locally unique smooth function $\boldsymbol{\xi}_{h,\mathbf{f}}(\boldsymbol{\mu})$, such that $\boldsymbol{\xi}_{h,\mathbf{f}}(\mathbf{0})=\mathbf{0}$ and

$$\mathbf{P}_{h,\mathbf{f}}\left(\boldsymbol{\xi}_{h,\mathbf{f}}(\boldsymbol{\mu}),\boldsymbol{\mu}\right)=\boldsymbol{\xi}_{h,\mathbf{f}}(\boldsymbol{\mu}) \tag{55}$$

for $\boldsymbol{\mu}\approx\mathbf{0}$. Derivatives of $\boldsymbol{\xi}_{h,\mathbf{f}}$ with respect to $\boldsymbol{\mu}$ evaluated at $\mathbf{0}$ may again be obtained through implicit differentiation. In this case,

$$\pi_k(\boldsymbol{\mu})=k\left(\boldsymbol{\xi}_{h,\mathbf{f}}(\boldsymbol{\mu}),\boldsymbol{\mu}\right) \tag{56}$$

denotes the local minimum in the value of k along a trajectory segment of $\boldsymbol{\Phi}_{\mathbf{f}}$ through $\boldsymbol{\xi}_{h,\mathbf{f}}(\boldsymbol{\mu})$ given the parameter vector $\boldsymbol{\mu}$. Derivatives of π_k with respect to $\boldsymbol{\mu}$ evaluated at $\mathbf{0}$ are again obtained by the use of the chain rule. In particular, $\boldsymbol{\xi}_{h,\mathbf{f}}(\boldsymbol{\mu})$ intersects $k=0$ at $\mathbf{0}$ transversally with respect to changes in $\boldsymbol{\mu}$ along a direction $\Delta\boldsymbol{\mu}$ provided that

$$\partial_{\boldsymbol{\mu}}\pi_k\cdot\Delta\boldsymbol{\mu}=\left(\partial_{\mathbf{x}}k\cdot\left(\mathbf{I}_n-\partial_{\mathbf{x}}\mathbf{P}_{h,\mathbf{f}}\right)^{-1}\cdot\partial_{\boldsymbol{\mu}}\mathbf{P}_{h,\mathbf{f}}+\partial_{\boldsymbol{\mu}}k\right)\cdot\Delta\boldsymbol{\mu}\neq 0. \tag{57}$$

In the degenerate case that equality holds, the nature of the extremum in π_k is determined by the sign of the quantity

$$\Delta\boldsymbol{\mu}^{\mathrm{T}}\cdot\partial_{\boldsymbol{\mu}}^2\pi_k\cdot\Delta\boldsymbol{\mu}=\partial_{\mathbf{x}}k\cdot\left(\mathbf{I}_n-\partial_{\mathbf{x}}\mathbf{P}_{h,\mathbf{f}}\right)^{-1}\cdot\begin{pmatrix}\Delta\boldsymbol{\xi}^{\mathrm{T}} & \Delta\boldsymbol{\mu}^{\mathrm{T}}\end{pmatrix}\cdot\begin{pmatrix}\partial_{\mathbf{xx}}\mathbf{P}_{h,\mathbf{f}} & \partial_{\mathbf{x}\boldsymbol{\mu}}\mathbf{P}_{h,\mathbf{f}}\\ \partial_{\boldsymbol{\mu}\mathbf{x}}\mathbf{P}_{h,\mathbf{f}} & \partial_{\boldsymbol{\mu}\boldsymbol{\mu}}\mathbf{P}_{h,\mathbf{f}}\end{pmatrix}\cdot\begin{pmatrix}\Delta\boldsymbol{\xi}\\ \Delta\boldsymbol{\mu}\end{pmatrix}, \tag{58}$$

where

$$\Delta\boldsymbol{\xi}=\left(\mathbf{I}_n-\partial_{\mathbf{x}}\mathbf{P}_{h,\mathbf{f}}\right)^{-1}\cdot\partial_{\boldsymbol{\mu}}\mathbf{P}_{h,\mathbf{f}}\cdot\Delta\boldsymbol{\mu}. \tag{59}$$

A.4. Near-grazing dynamics

Now suppose that $k\left(\boldsymbol{\Phi}_{\mathbf{f}}(\mathbf{0},\mathbf{0},t)\right)>0$ for $t\in\left(0,\tau_{h,\mathbf{f}}\right)$. Then, for $\mathbf{x}\approx\boldsymbol{\mu}\approx\mathbf{0}$ on $h=0$, the local dynamics corresponding to the piecewise smooth vector field (51) are equivalently represented by the composition $\mathbf{P}_{h,\mathbf{f}}\circ\mathbf{D}_{\mathbf{f},\mathbf{g}}$. In particular, provided that $k\left(\boldsymbol{\xi}_{h,\mathbf{f}}(\boldsymbol{\mu}),\boldsymbol{\mu}\right)>0$, it again follows that

$$\mathbf{P}_{h,\mathbf{f}}\left(\mathbf{D}_{\mathbf{f},\mathbf{g}}\left(\boldsymbol{\xi}_{h,\mathbf{f}}(\boldsymbol{\mu}),\boldsymbol{\mu}\right),\boldsymbol{\mu}\right)=\mathbf{P}_{h,\mathbf{f}}\left(\boldsymbol{\xi}_{h,\mathbf{f}}(\boldsymbol{\mu}),\boldsymbol{\mu}\right)=\boldsymbol{\xi}_{h,\mathbf{f}}(\boldsymbol{\mu}). \tag{60}$$

In contrast, for $\partial_{\mathbf{x}}k\cdot\Delta\mathbf{x}_2+\partial_{\boldsymbol{\mu}}k\cdot\Delta\boldsymbol{\mu}_2<0$, we have the result in Box I, where we recall that $\partial_{\mathbf{x}}k\cdot\Delta\mathbf{x}_1+\partial_{\boldsymbol{\mu}}k\cdot\Delta\boldsymbol{\mu}_1=0$. In this case, $\varepsilon\Delta\mathbf{x}_1+\varepsilon^2\Delta\mathbf{x}_2$ is a fixed point of the composition $\mathbf{P}_{h,\mathbf{f}}\circ\mathbf{D}_{\mathbf{f},\mathbf{g}}$ provided that

$$\Delta\mathbf{x}_1=\left(\mathbf{I}_n-\partial_{\mathbf{x}}\mathbf{P}_{h,\mathbf{f}}\right)^{-1}\cdot\partial_{\boldsymbol{\mu}}\mathbf{P}_{h,\mathbf{f}}\cdot\Delta\boldsymbol{\mu}_1 \tag{61}$$

and

$$\Delta\mathbf{x}_2=\partial_{\mathbf{x}}\mathbf{P}_{h,\mathbf{f}}\cdot\left(\Delta\mathbf{x}_2-\frac{4}{3}\sqrt{\frac{2}{\partial_{\mathbf{x}}h\cdot\mathbf{f}}}\left(-\partial_{\mathbf{x}}k\cdot\Delta\mathbf{x}_2-\partial_{\boldsymbol{\mu}}k\cdot\Delta\boldsymbol{\mu}_2\right)^{3/2}\times\left(\hat{\mathbf{g}}-\frac{\partial_{\mathbf{x}}h\cdot\hat{\mathbf{g}}}{\partial_{\mathbf{x}}h\cdot\mathbf{f}}\mathbf{f}\right)\right)+\partial_{\boldsymbol{\mu}}\mathbf{P}_{h,\mathbf{f}}\cdot\Delta\boldsymbol{\mu}_2+\frac{1}{2}\begin{pmatrix}\Delta\mathbf{x}_1^{\mathrm{T}} & \Delta\boldsymbol{\mu}_1^{\mathrm{T}}\end{pmatrix}\cdot\begin{pmatrix}\partial_{\mathbf{xx}}\mathbf{P}_{h,\mathbf{f}} & \partial_{\mathbf{x}\boldsymbol{\mu}}\mathbf{P}_{h,\mathbf{f}}\\ \partial_{\boldsymbol{\mu}\mathbf{x}}\mathbf{P}_{h,\mathbf{f}} & \partial_{\boldsymbol{\mu}\boldsymbol{\mu}}\mathbf{P}_{h,\mathbf{f}}\end{pmatrix}\cdot\begin{pmatrix}\Delta\mathbf{x}_1\\ \Delta\boldsymbol{\mu}_1\end{pmatrix}. \tag{62}$$

In particular, from (61) it follows that

$$\begin{aligned}\partial_{\boldsymbol{\mu}}\pi_k\cdot\Delta\boldsymbol{\mu}_1&=\left(\partial_{\mathbf{x}}k\cdot\left(\mathbf{I}_n-\partial_{\mathbf{x}}\mathbf{P}_{h,\mathbf{f}}\right)^{-1}\cdot\partial_{\boldsymbol{\mu}}\mathbf{P}_{h,\mathbf{f}}+\partial_{\boldsymbol{\mu}}k\right)\cdot\Delta\boldsymbol{\mu}_1\\&=\partial_{\mathbf{x}}k\cdot\Delta\mathbf{x}_1+\partial_{\boldsymbol{\mu}}k\cdot\Delta\boldsymbol{\mu}_1\\&=0,\end{aligned} \tag{63}$$

i.e., $\Delta\boldsymbol{\mu}_1$ must be chosen so that $\boldsymbol{\xi}_{h,\mathbf{f}}(\boldsymbol{\mu})$ intersects $k=0$ tangentially at $\mathbf{0}$ with respect to changes in $\boldsymbol{\mu}$ along the direction $\Delta\boldsymbol{\mu}_1$.

In the special case that $\Delta\boldsymbol{\mu}_1=\Delta\mathbf{x}_1=\mathbf{0}$, the expression given in Box I reduces to the expression in Box II which agrees with the result in [28] (see also [32]). To the best of our knowledge, the expression given in Box I in the more general case of $\Delta\boldsymbol{\mu}_1$, $\Delta\mathbf{x}_1\neq\mathbf{0}$ with

$$\partial_{\mathbf{x}}k\cdot\Delta\mathbf{x}_1+\partial_{\boldsymbol{\mu}}k\cdot\Delta\boldsymbol{\mu}_1=\partial_{\mathbf{x}}h\cdot\Delta\mathbf{x}_1+\partial_{\boldsymbol{\mu}}h\cdot\Delta\boldsymbol{\mu}_1=0 \tag{64}$$

is original to this paper.

References

[1] R. García, R. Pérez, Dynamic atomic force microscopy methods, Surf. Sci. Rep. 47 (6-8) (2002) 197–301.
[2] F.J. Giessibl, Advances in atomic force microscopy, Rev. Modern Phys. 75 (3) (2003) 949–983.
[3] N. Jalili, K. Laxminarayana, A review of atomic force microscopy imaging systems: Application to molecular metrology and biological sciences, Mechatronics 14 (8) (2004) 907–945.
[4] C. Bustamante, D. Keller, Scanning force microscopy in biology, Phys. Today 48 (12) (1995) 32–38.
[5] H.G. Hansma, Surface biology of DNA by atomic force microscopy, Annu. Rev. Phys. Chem. 52 (2001) 71–92.
[6] S. Kasas, N.H. Thomson, B.L. Smith, P.K. Hansma, J. Miklossy, H.G. Hansma, Biological applications of the AFM: From single molecules to organs, International J. Imaging Syst. Technol. 8 (2) (1997) 151–161.
[7] B. Pignataro, L. Chi, S. Gao, B. Anczykowski, C. Niemeyer, M. Adler, H. Fuchs, Dynamic scanning force microscopy study of self-assembled DNA-protein nanostructures, Appl. Phys. A 74 (3) (2002) 447–452.
[8] M. Radmacher, R.W. Tillman, M. Fritz, H.E. Gaub, From molecules to cells: Imaging soft samples with the atomic force microscope, Science 257 (5078) (1992) 1900–1905.
[9] A.N. Round, M.J. Miles, Exploring the consequences of attractive and repulsive interaction regimes in tapping mode atomic force microscopy of DNA, Nanotechnology 15 (4) (2004) S176–S183.

[10] R. García, A. San Paulo, Dynamics of a vibrating tip near or in intermittent contact with a surface, Phys. Rev. B 61 (20) (2000) R13381–R13384.
[11] N. Hashemi, H. Dankowicz, M.R. Paul, The nonlinear dynamics of tapping mode atomic force microscopy with capillary force interactions, J. Appl. Phys. 103 (2008) 093512 1–6.
[12] N. Hashemi, M.R. Paul, H. Dankowicz, M. Lee, W. Jhe, The dissipated power in atomic force microscopy due to interactions with a capillary fluid layer, J. Appl. Phys. 104 (2008) 063518 1–5.
[13] A. San Paulo, R. García, Unifying theory of tapping-mode atomic-force microscopy, Phys. Rev. B 66 (4) (2002) 041406 1–4.
[14] L. Nony, R. Boisgard, J.P. Aime, Nonlinear dynamical properties of an oscillating tip-cantilever system in the tapping mode, J. Chem. Phys. 111 (4) (1999) 1615–1627.
[15] P.J. de Pablo, J. Colchero, M. Luna, J. Gómez-Herrero, A.M. Baró, Tip-sample interaction in tapping-mode scanning force microscopy, Phys. Rev. B 61 (20) (2000) 14179–14183.
[16] A. San Paulo, R. García, High-Resolution imaging of antibodies by tapping-mode atomic force microscopy: Attractive and repulsive tip-sample interaction regimes, Biophys. J. 78 (3) (2000) 1599–1605.
[17] K. Yagasaki, Nonlinear dynamics of vibrating microcantilevers in tapping-mode atomic force microscopy, Phys. Rev. B 70 (24) (2004) 1–10.
[18] W. van de Water, J. Molenaar, Dynamics of vibrating atomic force microscopy, Nanotechnology 11 (3) (2000) 192–199.
[19] J.P. Hunt, D. Sarid, Kinetics of lossy grazing impact oscillators, Appl. Phys. Lett. 72 (23) (1998) 2969–2971.
[20] S.I. Lee, S.W. Howell, A. Raman, R. Reifenberger, Nonlinear dynamics of microcantilevers in tapping mode atomic force microscopy: A comparison between theory and experiment, Phys. Rev. B, 66(11), pp. 115409 1–10.
[21] A. Sebastian, M.V. Salapaka, D.J. Chen, J.P. Cleveland, Harmonic and power balance tools for tapping-mode atomic force microscope, J. Appl. Phys. 89 (11) (2001) 6473–6480.
[22] S.Y. Chou, P.R. Krauss, W. Zhang, L. Guo, L. Zhuang, Sub-10 nm imprint lithography and applications, J. Vac. Sci. Technol. B 15 (6) (1997) 2897–2904.
[23] K. Wilder, C.F. Quate, B. Singh, R. Alvis, W.H. Arnold, Atomic force microscopy for cross section inspection and metrology, J. Vac. Sci. Technol. B 14 (6) (1996) 4004–4008.
[24] H. Dankowicz, Nonlinear dynamics as an essential tool for non-destructive characterization of soft nanostructures using tapping-mode atomic force microscopy, Philos. Trans. R. Soc. A 364 (1849) (2006) 3505–3520.
[25] X. Zhao, H. Dankowicz, Characterization of intermittent contact in tapping mode atomic force microscopy, ASME J. Comput. Nonlinear Dyn. 1 (2) (2006) 1–7.
[26] H. Dankowicz, X. Zhao, S. Misra, Near-grazing dynamics in tapping-mode atomic-force microscopy, Internat. J. Non-Linear Mech. 42 (4) (2007) 697–709.
[27] A.B. Nordmark, Non-periodic motion caused by grazing indicidence in an impact oscillator, J. Sound Vibration 145 (2) (1991) 279–297.
[28] H. Dankowicz, A.B. Nordmark, On the origin and bifurcations of stick-slip oscillations, Physica D 136 (3–4) (2000) 280–302.
[29] M. Golubitsky, D.G. Schaeffer, Singularities and Groups in Bifurcation Theory, Springer-Verlag, New York, 1985.
[30] M. di Bernardo, C.J. Budd, A.R. Champneys, Grazing and border-collision in piecewise-smooth systems: A unified analytical framework, Phys. Rev. Lett. 86 (12) (2001) 2553–2556.
[31] M. di Bernardo, C.J. Budd, A.R. Champneys, Normal form maps for grazing bifurcations in n-dimensional piecewise-smooth dynamical systems, Physica D 160 (3-4) (2001) 222–254.
[32] M. di Bernardo, C.J. Budd, A.R. Champneys, P. Kowalczyk, Piecewise-smooth Dynamical Systems, Springer-Verlag, London, 2008.
[33] R.I. Leine, D.H. van Campen, B.L. van de Vrande, Bifurcations in nonlinear discontinuous systems, Nonlinear Dynam. 23 (2) (2000) 105–164.
[34] S. Foale, S.R. Bishop, Bifurcations in impact oscillations, Nonlinear Dynam. 6 (3) (1994) 285–299.
[35] R.W. Stark, G. Schitter, M. Stark, R. Guckenberger, A. Stemmer, State-space model of freely vibrating and surface-coupled cantilever dynamics in atomic force microscopy, Phys. Rev. B 69 (8) (2004) 085412 1–9.
[36] J. Lim, B.I. Epureanu, Multimode dynamics of atomic-force-microscopy tip-sample interactions and application of sensitivity vector fields, Proc. SPIE 6529 (2) (2007) art. 65293Y.
[37] H. Dankowicz, P. Piiroinen, A.B. Nordmark, Low-velocity impacts of quasiperiodic oscillations, Chaos Solitons Fractals 14 (2) (2002) 241–255.
[38] P. Thota, H. Dankowicz, Continuous and discontinuous grazing bifurcations in impacting oscillators, Physica D 214 (2) (2006) 187–197.
[39] H. Yabuno, H. Kaneko, M. Kuroda, T. Kobayashi, Van der Pol type self-excited micro-cantilever probe of atomic force microscopy, Nonlinear Dynam. 54 (1–2) (2008) 137–149.
[40] H. Dankowicz, J. Jerrelind, Control of near-grazing dynamics in impact oscillators, Proc. Roy. Soc. A 461 (2063) (2005) 3365–3380.
[41] H. Dankowicz, F. Svahn, On the stabilizability of near-grazing dynamics in impact oscillators, Internat. J. Robust Nonlinear Control 17 (15) (2007) 1405–1429.
[42] X. Zhao, H. Dankowicz, Control of impact microactuators for precise positioning, J. Comput. Nonlinear Dynam. 1 (1) (2006) 65–70.
[43] F. Svahn, H. Dankowicz, Controlled onset of low-velocity collisions in vibro-impacting systems with friction, in: Proc. Roy. Soc. A (2009) (in press).